SnS$_2$/B$_4$C@OUCNTs as a high-performance anode material for lithium-ion batteries

Wei Su[1] · Yandong Xie[1] · Kaidan Wu[1] · Deping Xiong[1] · Li Chen[1] · Zuyong Feng[1] · Kunhua Wen[1] · Zhaoying Li[2] · Miao He[1]

Abstract

The world's energy supply depends heavily on lithium-ion batteries due to the progressive depletion of non-renewable resources. The issue of raising the energy density of lithium-ion batteries must be addressed. We are all aware that the anode material is one area where lithium-ion batteries still have room for development. A new anode material, tin disulfide, not only has a high theoretical specific capacity (645 mAh g^{-1}), but also allows the formation of different microstructures through variable growth rates. In this study, we created three-dimensional nano-spheres of SnS$_2$ using solid-phase synthesis and then wrapped SnS$_2$ and B$_4$C in OUCNTs (SnS$_2$/B$_4$C@OUCNT) using hydrothermal synthesis. Ascribed to the synergy between the highly chemical active B$_4$C and the conductive carbon network of the OUCNTs, SnS$_2$/B$_4$C@OUCNT (149 Ω) effectively overcomes the drawback of high impedance of pure SnS$_2$ (307 Ω) while exhibiting high capacity and cyclic stability. After 100 cycles at a current density of 100 mA g^{-1}, this material displayed good electrochemical properties as the anode for lithium-ion batteries, obtaining a reversible capacity of 1024.7 mAh g^{-1} and a coulombic efficiency of 98.01%. The discharge capacity is 854.7 mAh g^{-1} with a coulombic efficiency of 98.57% after 200 cycles at 1000 mA g^{-1}.

Keywords Tin disulfide · Boron carbide · Oxidative unzipped multi-walled carbon nanotubes · Lithium-ion battery · Anode material

Introduction

Due to the stark incongruity between the rising demand for fossil fuels and the ever-harsher greenhouse gas emissions standards, it is crucial for humans to create and employ high-energy–density rechargeable batteries today [1–5]. While traditional and commercial lithium-ion batteries (LIBs) have cheap cost, extended cycle stability, and vast storage using graphite as the electrode materials, their limited property (372 mAh g^{-1}) and subpar rate capacity narrow their potential to advance [6]. Therefore, there has been growing interest in exploring ideal electrode materials with superior electrochemical performance. The unique physicochemical properties of the transition metal disulfides have sparked an increase in research activity in recent years due to a variety of possible uses, including energy storage, catalysts, and electronics. Additionally, due to the Li-ion conversion or alloying storage mechanism reaction, such as SnS$_2$, WS$_2$, MoS$_2$, and VS$_2$ [7], their theoretically specific capacity is larger than that of conventional plug-in electrode materials [8–11]. Among these diverse active materials, SnS$_2$ has a layered CdI2-type model, similar to graphene, and is held together by weak van der Waals interactions. Sn atom layers are situated between two levels of S atom layers. [12]. SnS$_2$ has a greater specific capacity than other metal disulfides like MoS$_2$ and WS$_2$, which may be attributed to the special processes of the conversion and Li-Sn alloying/dealloying [13]. During course of the reaction, SnS$_2$ demonstrates a high theoretically specific capacity (645 mAh g^{-1}) [14], and has been investigated as a potential contender for LIBs electrode material.

✉ Miao He
herofate666@126.com

1 School of Physics and Optoelectronic Engineering, Guangdong University of Technology, Guangzhou, Guangdong 510006, People's Republic of China

2 Zhongshan Engineering Laboratory of Micro-Integrated LED Packaging Technology, Zhongshan Mulinsen Electronics Company Limited, Zhongshan, Guangdong 528415, People's Republic of China

Despite the fact that diverse SnS_2 nanostructures have been utilized as active electrodes, the limited electronic conductivity of SnS_2 prevents their application in electrochemistry, particularly at high rates [15]. During charge/discharge cycles, the enormous volume change of SnS_2 would cause rapid capacity loss [16]. In order to get over these restrictions, it has been claimed that SnS_2 has been mixed with a variety of carbon materials, including carbon coatings, carbon nanotubes, and graphene [17–21]. Youn et al. synthesized the matrix composite of nitrogen-doped graphene oxide reduction and nanocrystals tin sulfides as lithium-ion battery anodes which showed good performance with expansion ratio reduced by 28%, retaining a reversible capacity of 562 mAh g^{-1} at the 200th loop at 0.2 A g^{-1} rate [22]. Yin et al. established the "double-sandwich-like" framework of SnS_2-reduced graphene oxide hybrid composite, which demonstrated superlative electrochemical performance, including a high initial or reversible discharge capacity and outstanding cyclic stability with superb coulombic efficiency of ~96.9% [23]. Kim et al. prepared the carbon-coated SnS_2 nanoparticles with a thickness of carbon coating about 5 nm which reduce volume change during the battery running process, so following 50 rounds, the reversal capacity was 668 mAh g^{-1} with a superior rate property [24]. As a result, carbon materials have the ability to lessen volume expansion caused by special layer structure in addition to improving electron transport. Among them, multi-walled carbon nanotubes are one of the important carbon-based materials whose mechanical and electronic properties depend on the structure, and researchers have been working to selectively improve its performance in certain aspects by blending its structure to meet specific needs. For example, the oxidative unzipping of multi-walled carbon nanotubes using a mixture of H_2SO_4 and $KMnO_4$ allows multi-walled carbon nanotubes to unfold along the axial direction, obtaining a larger specific surface area and more active sites while bonding a large number of oxygen functional groups at the edges and surfaces [25]. Therefore, oxidative unzipping multi-walled carbon nanotubes have good dispersion and conductivity and are suitable as carbon carriers for SnS_2.

Even so, researchers are still keen to find more novel electrode materials to a greater electrochemical performance boost. Boron carbide (B_4C) is a lightweight, reasonably priced refractory ceramic material [26]. As a result of its great resistance to general corrosion, it may provide an excellent active area for cells such lithium-oxygen, lithium-sulfur, and lithium-ion batteries [27–29]. Chen et al. created a Si/B_4C combination with a graphite covering that has an entire structure to increase the transport properties and durability of the rechargeable batteries. This combination exhibits outstanding cyclability by including a theoretical capacity of 822 mAh g^{-1} with 94% capacity retention after 100 cycles at 0.3 C charge/discharge speed [30]. Due to its

light weight ($\approx$2.5 g cm^{-3}), strong conductance, and superior catalytic action, B_4C is a suitable choice for electrochemical devices [26], good conductivity, and superior catalytic effect. To the best of our knowledge, B_4C is only very seldom used in rechargeable batteries, despite having thrived and grown. In addition, B_4C has been used as a raw material for anodes in sodium ion batteries and has achieved excellent electrochemical performance [31]; thus, the integration of B_4C into tin-based anode materials for lithium-ion batteries is a very worthy study subject.

In this study, we described a straightforward hydrothermal technique for the synthesis of 3D $SnS_2/B_4C@OUCNT$, in which many nanoflakes-assembly flower-shaped SnS_2 nanomaterials and evenly distributed B_4C were wrapped in oxidative unzipped multi-walled carbon nanotube films (OUCNTs), where highly conductive B_4C is used as a filling agent added to flower-shaped SnS_2 and also as a conductive connector between SnS_2 and OUCNTs. The severe tension brought on by the lattice expansion caused the longitudinal dimension of CNTs to modestly open under the combined action of sulfuric acid and oxidant molecules [32]. The undamaged core CNTs were kept as the framework of electronic transmission at this time. In order to intercalate lithium cations, the target product develops a three-dimensional space that offers more active surface area than the control sample. As a result, the lithium-ion battery with an optimized SnS_2 anode electrode produced a discharge capacity of 1840 mAh g^{-1} at 100 mA g^{-1} rate.

Experimental section

Chemical materials

The following chemicals were used in the synthesis of SnS_2 and $SnS_2/B_4C@OUCNTs$: stannous chloride dihydrate ($SnCl_2·2H_2O$, 98%), thiourea (H_2NCSNH_2, AR), absolute ethanol (CH_3CH_2OH, 99.7%), multi-walled carbon nanotubes (C139835, inner diameter: 5–10 nm, outer diameter: 20–30 nm, length: 10–30 μm), boron carbide (B_4C, 99%).

SnS_2 preparation

In an agate mortar, 2.25 g $SnCl_2·2H_2O$ and 1.9 g thiourea were placed, where they were uniformly ground into off-white powdery mixture for 30 min. Then, the mixture was moved into 50-mL corundum crucible without cover reacting at 180 °C in the air blast drying oven for 2 h. After cooling, the composition was soaked in distilled water standing for 10 h. The solids were then separated and extracted using centrifugation, which was carried out repeatedly with absolute ethanol and deionized water. By drying at 80 °C in air, the yellow product SnS_2 was finally gained.

Preparation of SnS$_2$/B$_4$C@OUCNTs

The oxidative unzipped MWCNTs were synthesized as previously reported [33]. For 3 h, 0.125 g OUCNTs were ultrasonically dispersed in 60 mL ethanol. For 24 h, 0.0625 g SnS$_2$ and 0.0125 g B$_4$C were added into OUCNTs dispersion stirring. The aforementioned dispersion was then transferred to a 100-mL Teflon reactor, heated to 180 °C, and allowed to react for 12 h. The black precipitate that was eventually formed was then cooled to room temperature and repeatedly cleaned with deionized water and absolute ethanol. The target product, SnS$_2$/B$_4$C@OUCNTs, was ultimately successfully abstained by drying it for 12 h at 60 °C in a low-pressure vacuum oven. The SnS$_2$@OUCNTs, for comparison, was created via a hydrothermal technique under identical conditions without the inclusion of B$_4$C.

Assembly of battery

The half-cell lithium-ion battery (LIBs) configuration was assembled so as to examine the electrochemical performance of SnS$_2$/B4C@OUCNTs composite material. SnS$_2$, SnS$_2$@OUCNTs, and SnS$_2$/B$_4$C@OUCNTs are respectively mixed with conductivity (SUPER P) and polyvinylidene fluoride (PVDF) in a mass ratio of 7:1.5:1.5 to obtain three kinds of homogenous slurry with N-methylpyrrolidone (NMP) solvent. After drying in vacuum for 12 h, the dried slurry was cut into discs and adheres to the copper foil with a slurry of approximately 100 μm. The disc and lithium foil were used as the working electrode and the counter electrode, respectively. The Celgard 2200 was acted as the separator, and 1 M LiPF6 mixed with EC and DMC (1:1, v/v) (DodoChem, Suzhou, China) was used as the electrolyte. Assembly of the coin cell (CR2032) was carried out in a glove box with

argon gas. Finally, discharge and charge measurements are performed by using LAND for testing.

Results and discussions

Physico-descriptive information

The SnS$_2$/B$_4$C@OUCNTs is prepared as shown in Fig. 1. The stannous chloride dihydrate compound was first ground with thiourea for 30 min into a homogeneous off-white powder, then transferred to a corundum crucible, and reacted by heating at 180 °C for 2 h to produce 3D SnS$_2$ microspheres. A dispersed aqueous solution of OUCNTs was combined with SnS$_2$ and B$_4$C, and the mixture was constantly agitated for 24 h using a magnetic stirrer. A stainless steel hydrothermal synthesis reactor was then used to develop the homogenous solution into 3D materials, with OUCNTs wrapping SnS$_2$ nanoballs and B$_4$C, under high pressure and temperature conditions [34].

Scanning electron microscopy (SEM) and high-resolution transmission electron microscopy (HRTEM) were employed for characterization in order to more thoroughly examine the microscopic appearance and structure of the mixture. The SEM picture of pure SnS$_2$ is shown in Fig. 2a, which depicts microspheres made of a number of tightly assembled two-dimensional SnS$_2$ sheets. The gaps between the layers of the sheets facilitate the storage of electrons or lithium ions in the battery during charging and discharging [35]. But SnS$_2$ has obvious shortcomings as an anode material for lithium-ion batteries, such as poor electrical conductivity, low energy storage density, and unstable long-term cycling. Figure 2b shows the SEM image of SnS$_2$@OUCNTs, which shows that SnS$_2$ grows wildly on OUCNTs, thereby improving the poor

Fig. 1 Schematic illustration of SnS$_2$/B$_4$C@OUCNTs fabrication

SnS$_2$/B$_4$C@OUCNTs

SnCl$_2$·2H$_2$O   thiourea   SnS$_2$ B$_4$C   OUCNTs
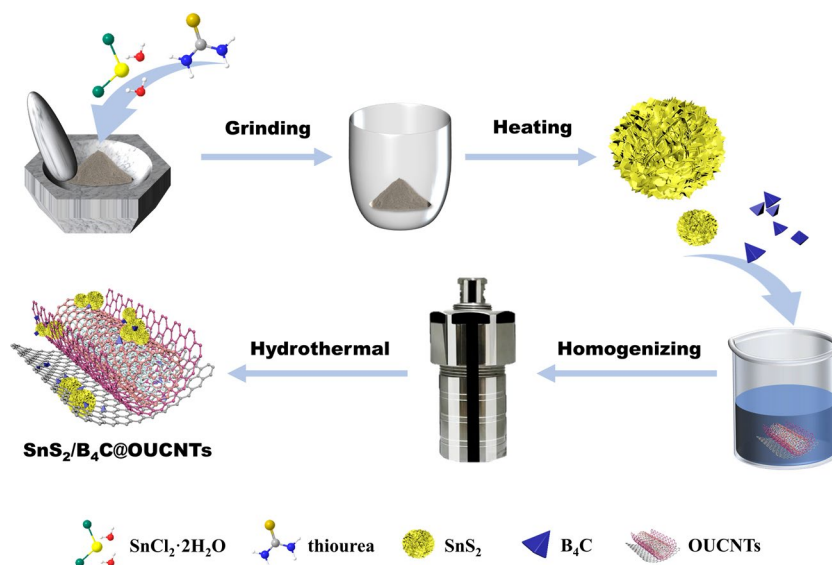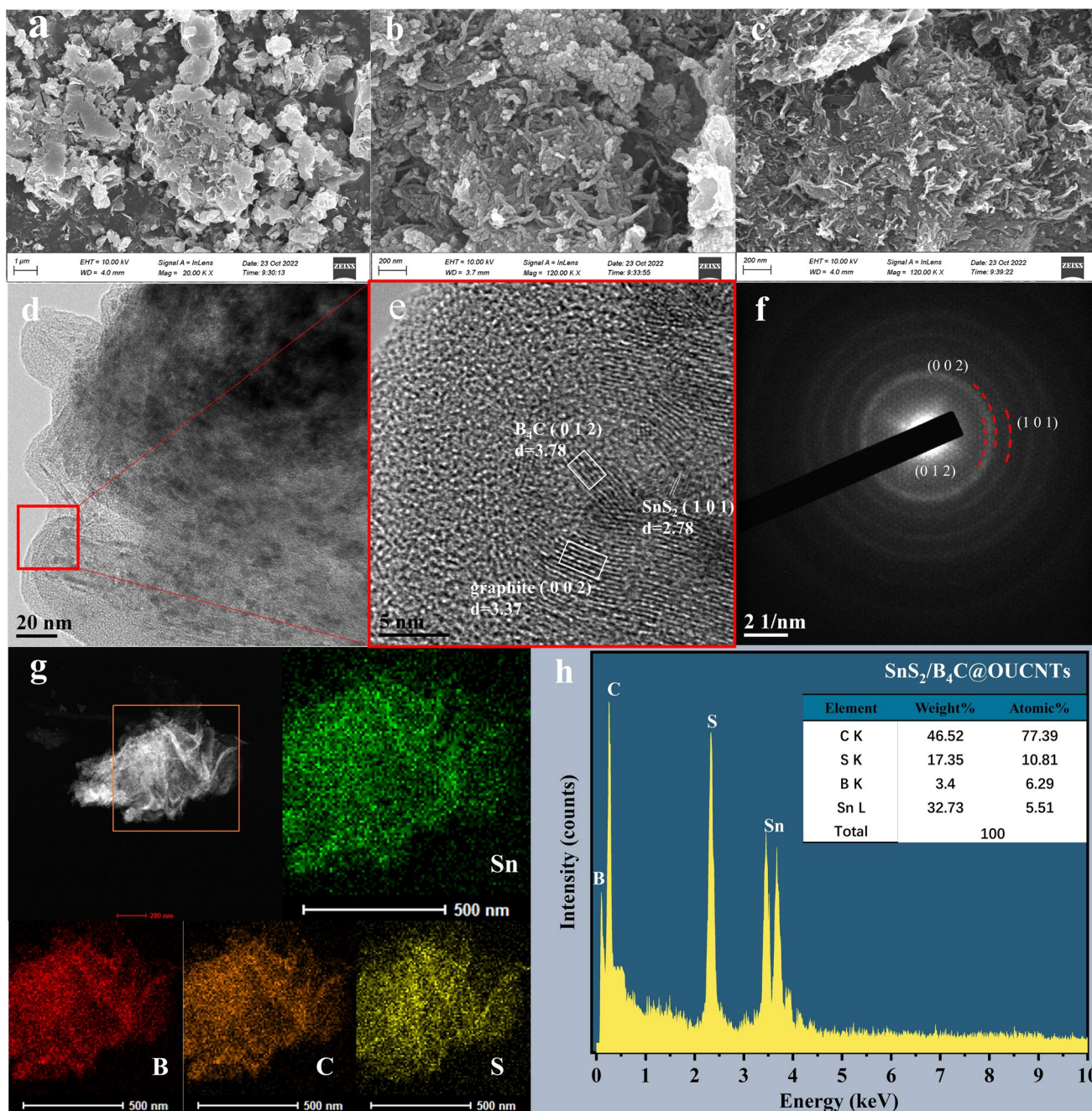
Fig. 2 **a–c** SEM images of pure SnS_2, SnS_2@OUCNTs, and SnS_2/B_4C@OUCNTs, respectively; **d–f** the HRTEM, **g** elemental mapping images, and **h** EDX spectrum of SnS_2/B_4C@OUCNTs electrode material

electrical conductivity of pure SnS_2. The extended growth of SnS_2 nanosheets on OUCNTs is shown in Fig. 2c, showing the microscopic morphology of SnS_2/B_4C@OUCNTs, which successfully mitigates the disadvantage of SnS_2's weak electrical conductivity [36]. At the same moment, the partially exposed OUCNTs indicate that SnS_2 nanosheets are present on the carbon matrix in moderate amounts, allowing the OUCNTs to still retain the function of storing electrons of ions. In terms of the overall structure, it offers

enough room for electrolyte penetration and shortens the Li-ion transport path, strengthening the Li-ion's adsorption capability and electrochemical characteristics. Therefore, this structure has the potential to further improve the rate performance of the battery.

Figure 2d is a TEM image of the composite SnS_2/B_4C@OUCNTs, revealing the intertwined OUCNTs that form a conductive carbon network wrapping around SnS_2 and B_4C. Additionally, Figure S1 illustrates the outer layers of the

multi-walled carbon nanotubes being axially oxidative cut and opened, thus creating additional anchoring sites for SnS_2 and B_4C and improving the integrity of the composite [32, 37]. Figure 2e further shows HRTEM image of $SnS_2/B_4C@$ OUCNTs, clearly showing the lattice edges of SnS_2 and B_4C as well as the enlarged carbon layers. Notably, the interlayer spacing of 2.78 nm corresponds to the (101) crystal plane of SnS_2, 3.78 nm to the (012) crystal plane of B_4C, and 3.37 nm to the (002) crystal plane of the carbon layer. In addition, Fig. 2e shows that SnS_2 and B_4C are highly encapsulated by the oxidative unzipped multi-walled carbon nanotubes. The (012) face of B_4C, the (002) face of the OUCNTs, and the (101) face of SnS_2 are all visible in the matching selected area electron diffraction (SAED) pattern, which supports the polycrystalline nature of the trapped B_4C and SnS_2 with such a different orientation (Fig. 2f).

Figure 2g shows the elemental mapping images of the $SnS_2/B_4C@$OUCNTs, which shows that the composites are homogeneous. The homogenous distribution of the components Sn, B, C, and S is seen in Fig. 2g. SnS_2 and B_4C have apparently been effectively wrapped and disseminated in the network by the OUCNTs, as evidenced by the uniform distribution of Sn and B on the carbon network framework created by the OUCNTs. In addition, the uniform dispersion of B element in the composite (Fig. 2g) indicates that the three materials, SnS_2, B_4C, and OUCNTs, are well bonded and can synergistically bring out the advantages of each other. Energy-dispersive X-ray microanalysis (EDX) was used to further analyze the content of C, S, B, and Sn elements in $SnS_2/B_4C@$OUCNTs, and the results are shown in Fig. 2h. After quantitative analysis, the proportions of C, S, B, and Sn in $SnS_2/B_4C@$OUCNTs can be estimated to be ~46.52%, ~17.35%, ~3.40%, and ~32.73%, respectively, which are revealed the probable experimental ratio of final product ($SnS_2:B_4C:$OUCNTs = 10:1:9).

X-ray photoelectron spectroscopy (XPS) was carried out on the $SnS_2/B_4C@$OUCNTs to examine the chemical composition and bonding configuration of the composites. No additional impurities are seen in the entire XPS spectrum (Fig. 3a), which displays signals for Sn, O, C, B, and S. Two distinctive peaks can be seen in the high-resolution Sn 3d XPS spectrum (Fig. 3b), which correspond to Sn $3d_{5/2}$ and Sn $3d_{3/2}$ in Sn^{4+}, respectively, at 487.5 and 495.9 eV [38–40]. The high-resolution XPS spectrum of elemental boron is depicted in Fig. 3c. It is separated into two distinctive peaks at 187.5 and 188.7 eV, which stand for the B-C bonds in B_4C and the B-B bonds, respectively [41]. Three unique distinctive peaks with binding energies of 162.2, 163.8, and 165.0 eV, which correspond to S $2p_{3/2}$ and S $2p_{1/2}$ in S^{2-}, can be seen in the high-resolution S 2p XPS spectrum (Fig. 3d) [42, 43]. The three typical peaks in the high-resolution C 1 s XPS spectrum (Fig. 3e) have binding energies of 284.8, 285.6, and 288.5 eV, respectively, and

correspond to C–C bonds, C-O bonds, and O-C=O bonds [36, 44, 45]. It is thought that the oxygenated carbon produced during the hydrothermal treatment makes it easier for the SnS_2 nanosheets to be anchored and dispersed through chemical and physical processes.

Pure SnS_2, $SnS_2@$OUCNTs (Figure S2), and $SnS_2/B_4C@$ OUCNTs were subjected X-ray diffraction (XRD) examination to ascertain the structural properties of the composites. The $SnS_2/B_4C@$OUCNTs composite's XRD analysis pattern is depicted in Fig. 4a, where it displays the distinctive XRD diffraction peaks of the composite of hexagonal SnS_2 and rhombohedral hexahedral structured B_4C. These include the XRD peaks at 2θ values of 28.20°, 32.12°, 41.89°, 49.96°, 52.45°, 60.62°, and 70.33° that are in accordance with the JCPDS data (JCPDS card number: 23–0677) and represent the (100), (101), (102), (110), (111), (201), and (113) crystal planes of hexagonal SnS_2. In addition, the typical diffraction peaks at 2θ values of 24.50°, 35.96°, 57.55°, 64.66°, and 76.58° are consistent with the JCPDS data (JCPDS card number: 35–0798) and correspond to the (012), (104), (107), (125), and (217) crystal planes of B_4C, respectively. As can be seen from Figure S2, the $SnS_2@$OUCNTs (Figure S2b) with the addition of oxide-cut carbon nanotubes only retains mainly the diffraction peak positions of pure SnS_2 (Figure S2a), but its diffraction peak intensity is significantly reduced. In contrast, the $SnS_2/B_4C@$OUCNTs composite preserves the majority of the diffraction peaks of pure SnS_2 (Fig. S3a) while also adding some of the distinctive diffraction peaks of the dopant B_4C and reducing the strength of the diffraction peaks seen in SnS_2. However, this does not affect the fact that the characteristic diffraction peaks in Fig. 4a all have a sharp peak pattern, implying that the composite $SnS_2/B_4C@$OUCNTs have high crystalline properties. Furthermore, the figure demonstrates that SnS_2 and B_4C are together successfully composited and encapsulated in oxide-cut carbon nanotubes.

The composite $SnS_2/B_4C@$OUCNTs' molecular structure is further illuminated by the Raman spectroscopy study. The Raman characteristic peaks of C-atom crystals at 1300 cm^{-1} and 1580 cm^{-1}, respectively, are the D and G peaks. The G peak indicates in-plane stretching vibrations of the C-atom sp^2 hybridization, and the D peak represents defects in the C-atom lattice [46]. The inclusion of oxidative unzipped carbon nanotube films effectively raises the degree of graphitization of the material, as shown by the comparison of the Raman spectrum of $SnS_2@$OUC-NTs with an I_D/I_G of 0.96. However, when $SnS_2/B_4C@$ OUCNTs and $SnS_2@$OUCNTs are compared, the I_D/I_G increases to 1.02, showing that the addition of boron carbide enhances the degree of flaws in the material's faulty lattice and adds conductance and adsorption sites for lithium-ion store. Additionally, a pinnacle at 311 cm^{-1}, which is thought to be the A_{1g} pattern of the SnS_2 phase,
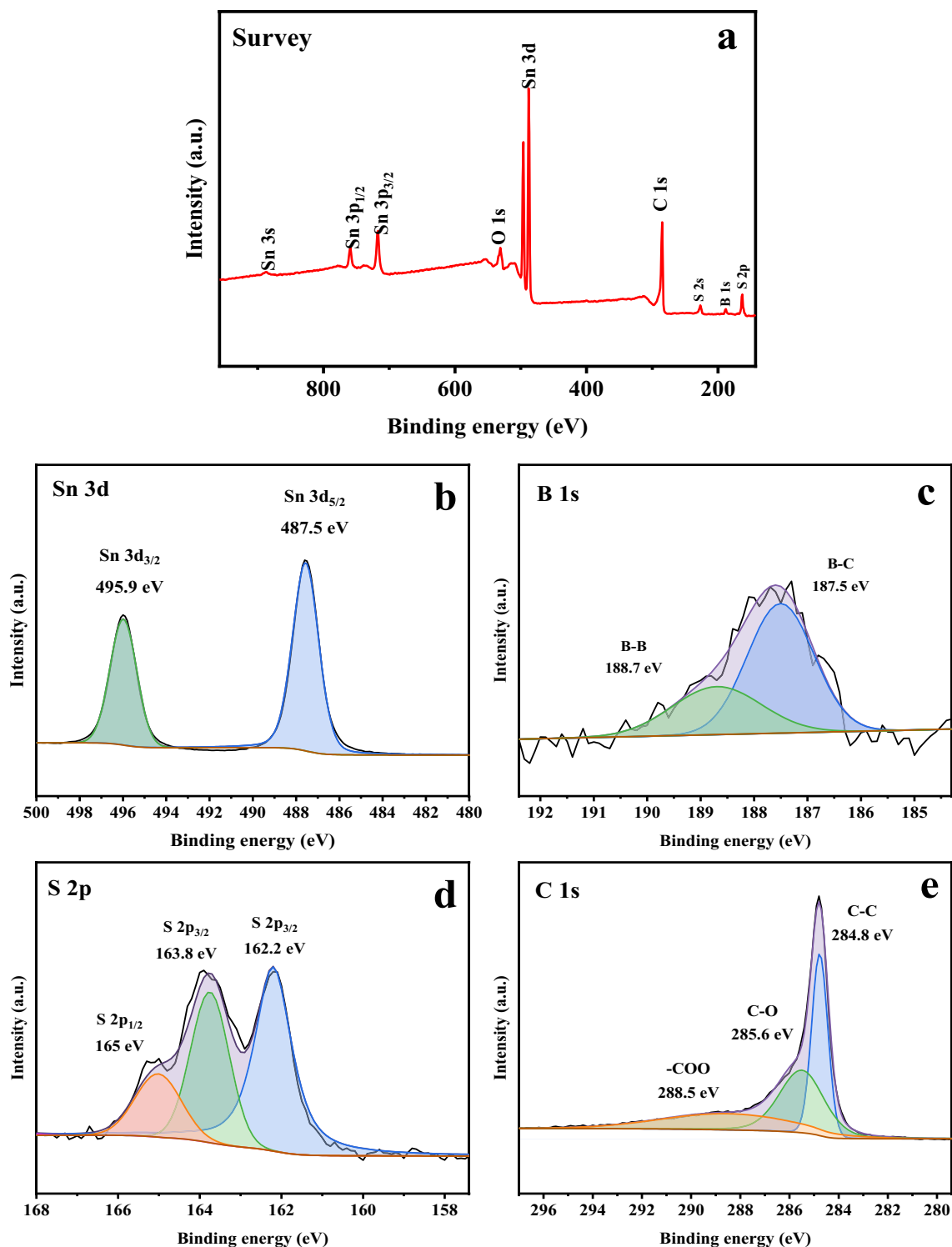
Fig. 3 **a** XPS survey spectrum and **b** Sn 3d, **c** B 1 s, **d** S 2p, and **e** C 1 s for SnS$_2$/B$_4$C@OUCNTs high-resolution spectra

can be seen in the Raman spectrum of SnS$_2$ [23, 47]. All Raman bands of SnS$_2$, B$_4$C, and OUCNTs can be seen in the Raman spectrum of SnS$_2$/B$_4$C@OUCNTs, confirming their inclusion in the composite.

SnS$_2$, SnS$_2$@OUCNTs, and SnS$_2$/B$_4$C@OUCNTs underwent Brunauer–Emmett–Teller (BET) and Barrett-Joyner-Halenda (BJH) studies to examine the specific surface area and pore structure of the materials. Figure 5a
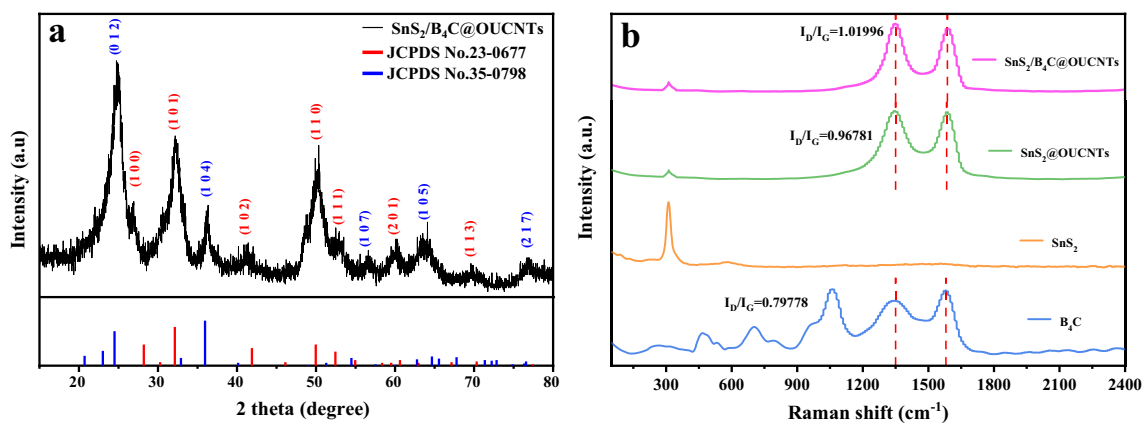
Fig. 4 **a** XRD pattern of SnS$_2$/B$_4$C@OUCNTs; **b** Raman spectra of SnS$_2$/B$_4$C@OUCNTs and comparative samples
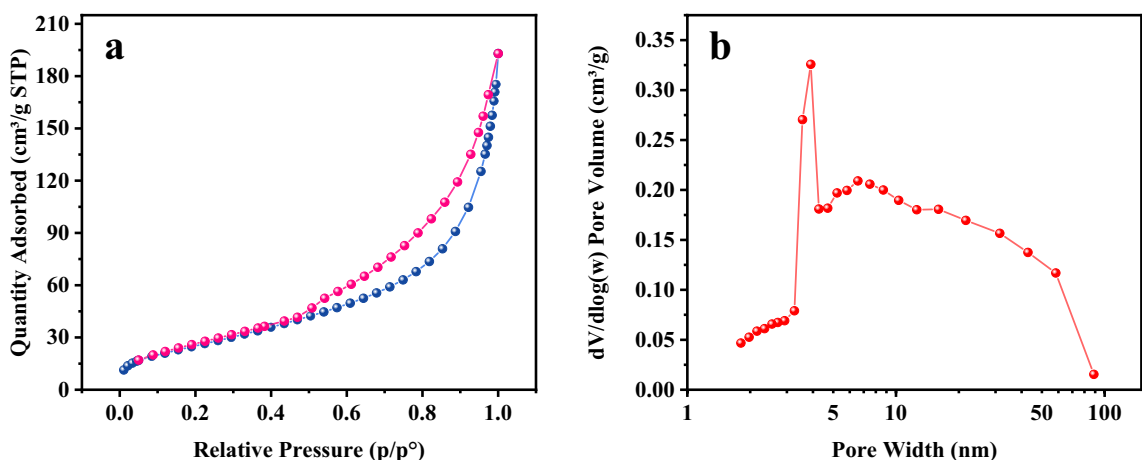

Fig. 5 **a** Adsorption–desorption isotherms and **b** BJH pore size distribution curve of SnS$_2$/B$_4$C@OUCNTs

illustrates the adsorption/desorption isotherms of nitrogen for SnS$_2$/B$_4$C@OUCNTs, which matches the characteristics of the type IV adsorption/desorption isotherm. The material is a lamellar material with mesopores, as indicated by the visible hysteresis loop of type H3 in the relative pressure range of 0.4 to 1.0 [48]. The specific surface area of SnS$_2$/B$_4$C@OUCNTs, determined by the BET method, is 94.23 m^2 g^{-1}, which falls between the other two samples, SnS$_2$ (40.96 m^2 g^{-1}) and SnS$_2$@OUCNTs (74.18 m^2 g^{-1}), as shown in Figure S3. The BJH pore size distribution of SnS$_2$/B$_4$C@OUCNTs is presented in Fig. 5b, clearly indicating that the material's pore sizes are concentrated in the mesoporous region. The increased contact area of the electrolyte with the materials enhances the migration channels for ions and shortens the routes, boosting the rate capability. This is facilitated by the moderate specific surface area and mesoporous structure of SnS$_2$/B$_4$C@OUCNTs. Additionally, reducing the formation of the SEI film may increase the initial coulombic efficiency of LIBs.

In addition, thermogravimetric (TGA) analysis was used in this work to determine the compositional content of SnS$_2$/B$_4$C@OUCNTs, which was heated in air from 30 to 800 °C at a ramp rate of 10 °C/min, as shown in Fig. 6. The 1.4% heat loss within ~200 °C is due to the evaporation of water and decomposition of oxygen-containing functional groups inside the material. Approximately 8.67% heat loss from 200 to 450 °C is mainly attributed to the oxidation of SnS$_2$ in air to form SnO$_2$, and ~45% heat loss occurring from 450 to 800 °C is mainly due to the oxidation of carbon material [33, 49]. After combining the EDX calculations, the contents of SnS$_2$, B$_4$C, and OUCNTs in SnS$_2$/B$_4$C@OUCNTs were obtained to be about 50%, 5%, and 45%, respectively.

D SnS$_2$/B$_4$C@OUCNTs electrochemical property

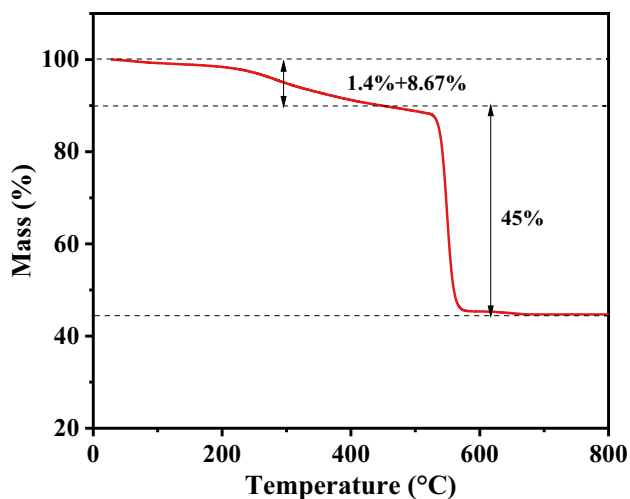The electrochemical property of LIB half-cell made from SnS$_2$/B$_4$C@OUCNTs electrode components was evaluated.

Fig. 6 TGA graph of SnS$_2$/B$_4$C@OUCNTs

In this case, the anode consisted of SnS$_2$/B$_4$C@OUCNTs, while the counter electrode (cathode) was made of lithium chips. First, cyclic voltammetry (CV) was used to

assess the half-cell between 0.01 and 3.0 V (versus Li$^+$/Li) at 0.1 mV s^{-1} scan rate. Figure 7a displays five initial CV curves. Five distinct reduction peaks with centers at 1.65 V, 1.3 V, 1.0 V, 0.71 V, and 0.2 V are shown in the initial cathodic scan curves. The first peak at 1.65 V results from the entrance of lithium into the SnS$_2$ interlayer without phase disruption, which corresponds to the conversion reaction (1), $SnS_2 + xLi^+ + xe^- \leftrightarrow Li_xSnS_2$ [50]. $Li_xSnS_2 + (4-x)Li^+ + 4.4e^- \leftrightarrow Sn + 2Li_2S$ (2) [51] is the conversion reaction mechanism that is responsible for the additional three reduction peaks at 1.3 V, 1.0 V, and 0.71 V. Due to the deterioration of the electrolyte, SnS$_2$ changes into Sn nanoparticles that are incorporated into the Li$_2$S substrate and create a solid electrolyte interface (SEI) [35]. The creation of the Li$_x$Sn alloy and the introduction of Li$^+$ into the oxidatively unzipped multi-walled carbon nanotubes were credited causing the peak of about 0.2 V. Three anodic peaks at 0.55 V, 1.89 V, and 2.37 V can be seen in the initial anodic scanning. The delithiation process of the Li$_x$Sn is visible in the oxidation peak at 0.55 V, accompanying by the reversible process of conversion reaction (2). And the reversible process of conversion
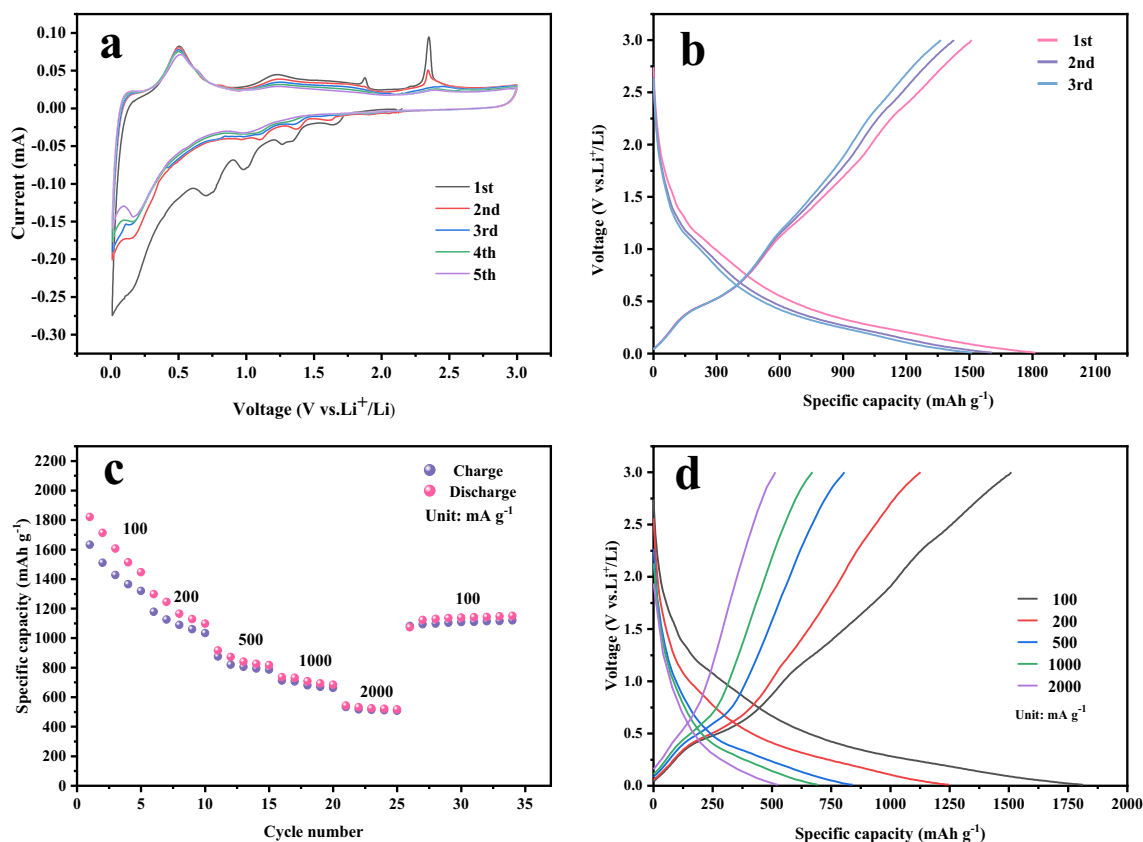

Fig. 7 SnS$_2$/B$_4$C@OUCNTs electrochemical characterization includes **a** CV curves at 0.1 mV s^{-1} scan rate, **b** charge/discharge curves at 100 mA g^{-1} current density, **c** rate performance at various current rates from 100 to 2000 mA g^{-1}, and **d** charge/discharge curves at various current rates from 100 to 2000 mA g^{-1}

reaction (1) causes the peak at 1.89 V, corresponding to the synthesis of SnS_2 and the partial Sn oxidation [52]. Lithium ions being removed from the SnS_2 sheet are likely what caused the oxidative peak around 2.37 V [53]. With the passage of scanning time, the other four laps gradually coincide which suggests that the lithium-ion half-cell with 3D $SnS_2/B_4C@OUCNTs$ composite as anode electrode possesses stable electrochemical property.

Figure 7b depicts the charge/discharge graphs of $SnS_2/B_4C@OUCNTs$ during the initial three cycles at a steady current density of 100 mA g^{-1}. The first three discharge processes have specific capacities of 1813.3, 1606.6, and 1513.3 mAh g^{-1}; meanwhile, the first three charge processes have specific capacities of 1510.6, 1426.6, and 1364.6 mAh g^{-1}. So the initial coulomb efficiency (ICE) of the $SnS_2/B_4C@OUCNTs$ is then calculated as 83.46%. In accordance with the initial CV finding, this lower ICE of the first electrochemical charge/discharge curve is attributed to the development of an SEI thin coating on the surface of active material. In second run, the corresponding coulombic efficiency value rises to 88.79%, and during the third run, it even reaches 90.17%. Additionally, depictions of the charging/discharging curves of SnS_2 (Figure S4a) and $SnS_2@OUCNTs$ (Figure S4b) at 100 mA g^{-1} for the first three turns, where the ICEs are 59.39% and 83.20%, respectively, reveal that the components of OUCNTs and B_4C may successfully raise the ICE of the active electrode, hence enhancing the materials' electrochemical performance. Furthermore, Fig. 7b demonstrates that the voltage plateau and the redox peak of the CV curve in Fig. 7a are related. The composite electrode made of SnS_2 and $B_4C@OUCNTs$ reached a voltage plateau during the first discharge process (lithiation course), which is consistent with the behavior of Li$^+$ when it embeds in the SnS_2 lamellas and undergoes transformation into Li_2S and Sn [54]. Then, the de-alloying of Li_xSn, degradation of Li_2S, oxidation of metal Sn, and creation of SnS_2 all occur at the voltage plateau of the initial charge process (sulfation course), according to research conducted [55].

Figure 7c shows the rate capability of the $SnS_2/B_4C@OUCNTs$ anode materials. The electrodes' discharging specific capacities are respectively 1511, 1126, 806, 706, and 514 mAh g^{-1} at 100, 200, 500, 1000, and 2000 mA g^{-1} current densities. It is interesting that after cycling at high current densities, the discharge specific capacity also recovers to 79.5% of the original specific capacity when the current density drops to 100 mA g^{-1}, demonstrating strong rate capability. By contrast, it shows the rate performances for pure SnS_2 and $SnS_2@OUCNTs$ in figure S5, where their discharge capacities respectively recover to 18.39% and 28.09% of the original specific capacities, much lower than the rate capability of $SnS_2/B_4C@OUCNTs$. As a result, $SnS_2/B_4C@OUCNTs$ exhibit high reversal capacity and durable cyclability as an anode material for LIBs.

The charge/discharge graphs of various current densities are displayed in Fig. 7d for $SnS_2/B_4C@OUCNTs$. High sweeping rates do not substantially alter the curve's shape, indicating that the $SnS_2/B_4C@OUCNTs$ anode has good rate performance. And below are the reasons for this exceptional property: (1) The unique oxidative unzipping of multi-walled carbon nanotube framework structure acts as a scaffold matrix to avoid collapsing and to offer a high active surface area, allowing for the fast passage of lithium ions in an unhindered manner [32, 37]. (2) The oxidating and unzipping of OUCNTs in $SnS_2/B_4C@OUCNTs$ materials incorporates hydrophilic functional groups, which improve the hydrophilicity of the active material and increase the contact area of the active electrode material and electrolyte to speed up the rate of chemical reaction [33]. (3) Electrochemical impedance spectroscopy (EIS) evidences that doping of conducting material B_4C lowers the resistivity of the $SnS_2/B_4C@OUCNTs$ composite materials [29]. Herein, the B_4C of active material also acts as a catalyst, which is responsible for the rapid synthesis and decomposition of SEI films during charging and discharging process, indirectly boosting the reversible capacity and long lifetime upon the working electrode.

With an original discharge specific capacity of 1840 mAh g^{-1} at 100 mA g^{-1}, $SnS_2/B_4C@OUCNTs$ (Fig. 8a) exhibit strong energy storage that is much better than that of SnS_2 (1188 mAh g^{-1}) (Figure S6a) and $SnS_2@OUCNTs$ (1640.8 mAh g^{-1}) (Figure S6b). After a further 100 cycles, the $SnS_2/B_4C@OUCNTs$ electrode's discharge specific capacity (1024.7 mAh g^{-1}) and coulombic efficiency (98.01%) remain steady and continue to increase. And the respective discharge specific capacities of SnS_2 and $SnS_2@OUCNTs$ drop to 85.1 mAh g^{-1} and 647 mAh g^{-1} after 100 cycles, with coulombic efficiencies of 98% and 95.66%. And the cycling performance graph of pure B_4C is provided in Figure S6c. The initial capacity of B_4C in is not high (445.8 mAh g^{-1}) and only 73.4 mAh g^{-1} reversible capacity remains after 100 cycles, so B_4C is not suitable as a LIBs' anode material alone. However, B_4C has catalytic effect and high conductivity, and the synergistic effect with SnS_2 and OUCNTs can make $SnS_2/B_4C@OUCNTs$ achieve better cycling performance. Figure 8b reveals that $SnS_2/B_4C@OUCNTs$ material has good cycling stability as the electrode material for lithium battery, maintaining a reversible capacity of 854.7 mAh g^{-1} at 1000 mA g^{-1} large current density with 98.57% coulombic efficiency after 200 turns of charging/discharging processes. In addition, the specific capacities of the cells have a certain degree of decrease during approximately the first 60 turns of the charging and discharging processes. This is because the electrode material and the electrolyte are in the process of reacting at the solid–liquid phase interface to form a SEI film, resulting in the lithium ions
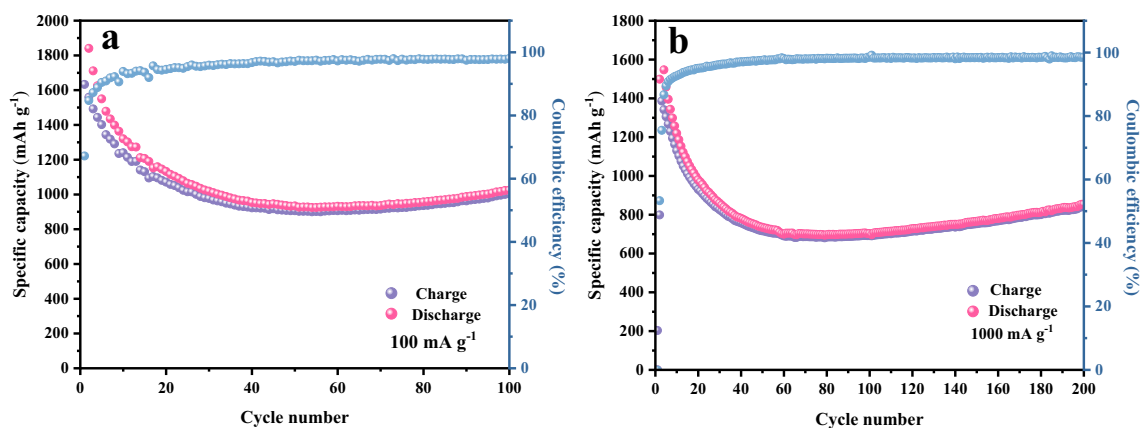
Fig. 8 **A**, **b** Cycling stability of composite electrodes made of $SnS_2/B_4C@OUCNTs$ at current densities of 100 mA g^{-1} and 1000 mA g^{-1}

not getting a normal standard. The upward trend in capacity is due to the construction of the SEI film and the expansion of the contact area between the electrode material and the electrolyte. Although the construction of the SEI film consumes a portion of the lithium ions to increase the irreversible capacity, the organic insolubility of the SEI film prevents solvent molecules from damaging the electrode material, greatly improving the cycling performance and service life of the electrode. And the recovery of capacity after about 60 cycles should be attributed to the increased interlayer spacing via activating material, increasing diffusion rate of Li^+ and lithium storage space [56]. This will help the material reduce the loss of irreversible capacity.

The CV curves of the material were kinetically studied to further understand the $SnS_2/B_4C@OUCNTs$' electrochemical characteristics and capacitive behavior. The CV curves for various sweeping rates, ranging from 0.1 to 1.0 mV s^{-1}, are shown in Fig. 9a. The $SnS_2/B_4C@OUC-NTs$ electrode demonstrates quick responsiveness since the CV curves' form essentially does not change over time. The connection of peak current (i) and sweeping rate (ν) provides insight into the electrochemical kinetics of the anode, according to Eq. (1) [57, 58]:

$$i = a\nu^b \tag{1}$$

where i represents the current of oxidation or reduction peak, ν represents the scan rate, and a and b serve as constants. Through Fig. 9a, Eq. (2) can be obtained by taking the logarithm for different voltage scan rates and corresponding peak current values in both sides of Formula (1):

$$\log(i) = b\log(\nu) + \log(a) \tag{2}$$

Consequently, b may be calculated by plotting the slope of the fitting $\log(i)$ versus $\log(\nu)$. In principle, diffusion-controlled cell properties are displayed by the electrode

material if $b = 0.5$, whereas capacity-controlled pseudo-capacity properties are displayed by the electrode material if $b = 1$.

The slopes of the linear connection of $\log(i)$ and $\log(\nu)$ from the peaks of the cathode and anode, respectively, are 0.657 and 0.666 in Fig. 9b. These findings imply that diffusion-controlled mechanisms and capacitive effects play a role in the electrochemical kinetics of the $SnS_2/B_4C@OUCNTs$ anode. Additionally, Formula (3) may be used to determine the contribution of the pseudo-capacity [59]:

$$i(V) = k_1\nu + k2\nu^{1/2} \tag{3}$$

where V is the specific voltage, k_1 and k_2 act as the fitting constants, ν is the scanning rate of specific voltage, and $k_1\nu$ and $k_2\nu^{1/2}$ are respectively the pseudo-capacity contribution and the diffusive contribution to the current at a given voltage. Figure 9c demonstrates that at scan speeds of 0.1–1.0 mV s^{-1}, the electrode's capacity contribution rises from 20 to 51%. The electrochemical action of the $SnS_2/B_4C@OUCNTs$ electrode is mostly controlled by diffusion at low current densities, whereas capacity control is more prominent at high current densities. Figure 9d shows the CV curve at 1.0 mV s^{-1} and the closed curve of the pseudo-capacity contribution via fitting analysis, where the pseudo-capacity contribution is calculated as 51%. Because of the unique $SnS_2/B_4C@OUCNTs$ coating structure and the flower-like structure of the B_4C-doped SnS_2, the capacitive contribution of Li^+ storage mechanism can gradually increase with increasing sweep rate. Thus, the strong capacity contribution, as a result of the short diffusion route and quick transmission speed for ions and electrons, is one of the reasons why $SnS_2/B_4C@OUCNTs$ electrode can sustain great performance at high sweeping rates.

The electrochemical impedance spectroscopy tests allow a better comparative investigation of the good performance
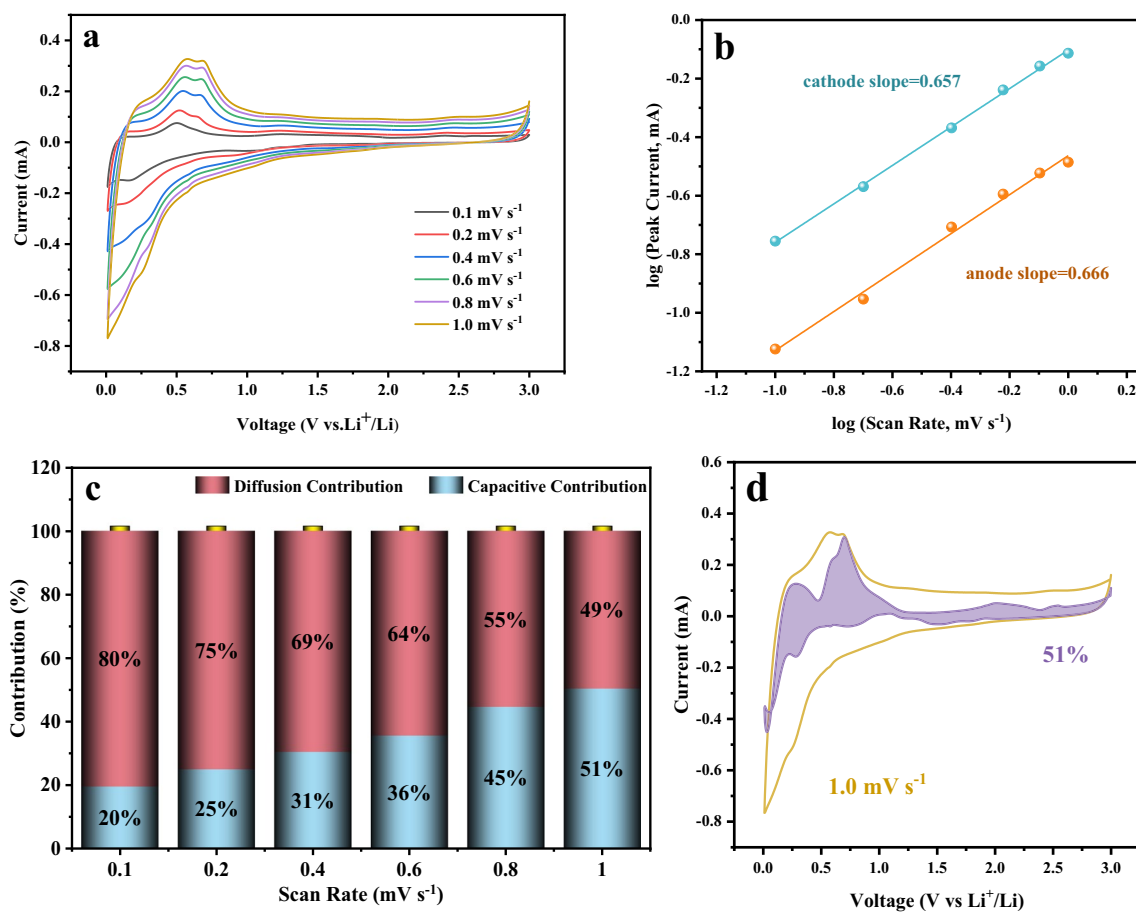
Fig. 9 **A** SnS$_2$/B$_4$C@OUCNTs CV curves at various scan rates; **b** a linear graph for log(i) vs. log(ν); **c** the ratio of diffusion and capacitive contributions at various sweeping rates; and **d** the capacitive contribution at 1.0 mV s^{-1}

of the SnS$_2$/B$_4$C@OUCNTs anode material. Meanwhile, by using a simulated equivalent circuit to match the electrochemical impedance spectra, it is possible to further examine the kinetic characteristics of the composite electrode. Figure 10d shows the fitted equivalent circuit model, where R_s stands for the resistance of the solution, electrode, and material; CPE and R_{ct} refer to the charge transfer impedance at the contact area between electrode and electrolyte; and Z_w is related to the Warburg impedance that is brought on by the diffusion of lithium ions. Figure 10a shows the Nyquist plots for three contrasting electrodes in which each curve consists of a tiny intercept point (R_s) and a semicircle of the high-frequency zone (R_{ct} and CPE) and a sloping line (Z_w) of the low frequency zone. In comparison to pure SnS$_2$ and SnS$_2$@OUCNTs, the semicircle of the SnS$_2$/B$_4$C@OUC-NTs electrode is obviously smaller. Obviously, the semicircle of the SnS$_2$/B$_4$C@OUCNTs composite is smaller than that of pure SnS$_2$ and SnS$_2$@OUCNTs. According to the fitting analysis, the fitted R_{ct} value of SnS$_2$/B$_4$C@OUCNTs is 149 Ω which is less than the fitted R_{ct} value of pure SnS$_2$ (307 Ω) and SnS$_2$@OUCNTs (150 Ω). This result clearly

confirms that SnS$_2$/B$_4$C@OUCNTs has a smaller transfer resistance while charging and discharging. To put it another way, the composite electrode made of SnS$_2$/B$_4$C@OUCNTs material exhibits quicker charge transfer kinetics, indicating that better ionic diffusive channels are crucial for increasing lithium-ion store.

Figure 10b shows three linearly fitted Warburg plots (Z′ vs. $\omega^{-1/2}$), which can obtain accurate Li-ion diffusion coefficients. The Warburg coefficient of the SnS$_2$/B$_4$C@OUCNTs composite electrode material is 170.76 Ω s^{-1}, which is much smaller than the Warburg coefficient of pure SnS$_2$ (780.19 Ω·s^{-1}) and SnS$_2$@OUCNTs (216.94 Ω·s^{-1}). And the diffusion coefficients of lithium ions are calculated by Eq. (4) as follows [60]:

$$D_{Li}^+ = \frac{R^2 T^2}{2A^2 n^4 F^4 C_o^2 \sigma_\omega^2} \tag{4}$$

where R denotes the gas constant, T stands for the absolute temperature, A signifies surface area of the electrode sheet, n represents the sum of shifting electrons, F means the
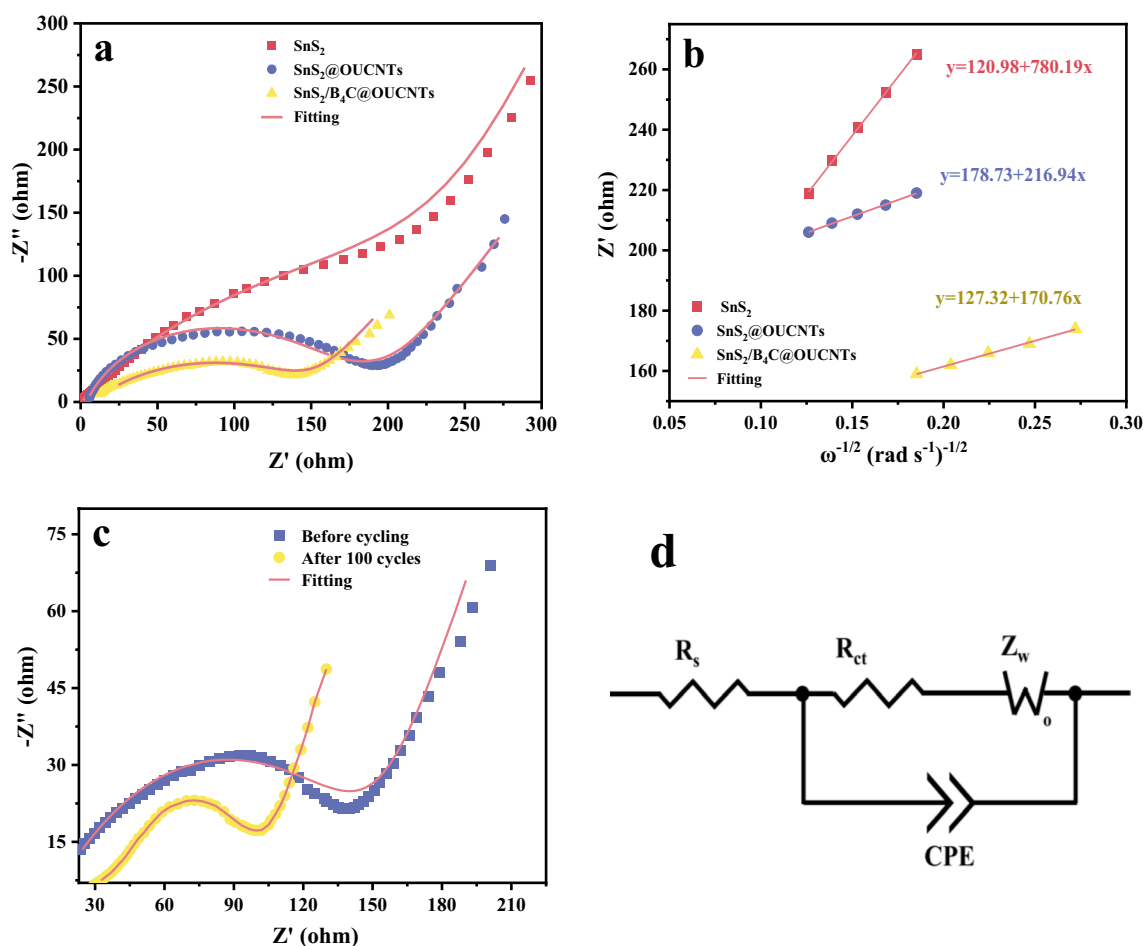
Fig. 10 a Nyquist plots and **b** the plots of Z′ versus $\omega^{-1/2}$ of SnS$_2$, SnS$_2$@OUCNTs, and SnS$_2$/B$_4$C@OUCNTs; **c** Nyquist plots of the SnS$_2$/B$_4$C@OUCNTs electrode after 100 cycles at 100 mA g^{-1}; **d** the equivalent circuit model for studied system

Faraday constant, C_o is the ionic molarity, and σ_ω expresses the Warburg coefficient. Formula (4) states that the Warburg coefficient, which is a deciding factor, has a square root relationship with the diffusion coefficient of lithium ions. SnS$_2$/B$_4$C@OUCNTs electrode has an estimated lithium-ion diffusion coefficient of 8.02×10^{-22} cm s^{-1}, which is greater than that of pure SnS$_2$ (3.83×10^{-23} cm s^{-1}) and SnS$_2$@OUCNTs (4.96×10^{-22} cm s^{-1}). Due to the high diffusion coefficient, the electrode performs well in terms of rate and charge/discharge even at large current densities. Consequently, the inclusion of OUCNTs and B$_4$C boosts not only the electron conductivity but also the speed at which electrons transfer in during insertion and release of lithium ions at high current densities, greatly enhancing the electrochemical properties of the SnS$_2$/B$_4$C@OUCNTs anode.

Moreover, Fig. 10c exhibits the comparison of electrochemical impedance spectra about the SnS$_2$/B$_4$C@OUCNTs composite electrode before and after 100 turns of charging/discharging at 100 mA g^{-1}. The semicircle in high-frequency zone of the impedance curve after cycling can be shown to be

substantially smaller than that of the impedance curve without cycling, showing that the resistance of SnS$_2$/B$_4$C@OUCNTs electrode's charge transmission will decrease after 100 cycles at 100 mA g^{-1}. Repeated studies have consistently shown that the integration of OUCNTs and B$_4$C plays a significant role in cycling, increasing the diffusion and transfer of lithium ions and electrons during cycling, and producing favorable electrochemical characteristics as a result.

In this work, SnS$_2$/B$_4$C@OUCNTs exhibits good cycling performance compared to the reported Sn-based sulfide-based electrodes for LIBs, and the comparisons are shown in Table 1. This result indicates that SnS$_2$/B$_4$C@OUCNTs is a potential and feasible anode material LIBs.

Conclusions

To sum up, three-dimensional oxidized chain-dissolved multi-walled carbon nanotubes encapsulating SnS$_2$ and B$_4$C were successfully synthesized by a straightforward

Table 1 Performance comparison of different electrode materials

Electrode materials	First reversible capacity (mAh g^{-1})	Current density (mA g^{-1})	Capacity retention (Nth) (mAh g^{-1})	Ref
CPN@SnS$_2$	1422	300	699.2 (100th)	[61]
LL-SnS$_2$/G	≈900	200	773.04 (180th)	[62]
SnS$_2$-SG	≈400	500	200 (1500th)	[34, 63]
Li$_2$S/Li$_x$Sn/NRGO	≈630	200	562 (200th)	[22]
HPC-SnS$_2$-PAN-500	≈800	500	652.5 (900th)	[64]
SnS$_2$/B$_4$C@OUCNTs	1547	1000	854.7 (200th)	This work

hydrothermal reaction. As an anode for LIBs, the results show that the SnS$_2$/B$_4$C@OUCNTs electrodes exhibit better cycling performance with a specific capacity retention of 1024.7 mAh g^{-1} cycling 100 times and higher rate performance with a high capacity of 854.7 mAh g^{-1} at 1000 mA g^{-1} than the pure phase SnS$_2$ and SnS$_2$@OUCNTs (85.1 mAh g^{-1} and 647 mAh g^{-1} after 100 cycles at 100 mA g^{-1}, respectively). This shows that the disadvantages of poor SnS$_2$ conductivity and capacity decay can be effectively improved by combining conductive yet flexible oxidative unzipping carbon nanotubes and highly chemically active boron carbide with nanosheet self-assembled SnS$_2$ and even has potential for usage for LIBs as the high-performance anode material.

The Supporting Information is available free of charge on the experimental section, TEM, XRD, BET, and electrochemical evaluation of the samples.

Declarations

Conflict of interest The authors declare no competing interests.

References

1. Di Lecce D, Verrelli R, Hassoun J (2017) Lithium-ion batteries for sustainable energy storage: recent advances towards new cell configurations. Green Chem 19:3442–3467. https://doi.org/10.1039/C7GC01328K

2. Dunn B, Kamath H, Tarascon JM (2011) Electrical energy storage for the grid: a battery of choices. Science 334:928–935. https://doi.org/10.1126/science.1212741

3. Jiao X, Liu Y, Li B, Zhang W, He C, Zhang C, Yu Z, Gao T, Song J (2019) Amorphous phosphorus-carbon nanotube hybrid anode with ultralong cycle life and high-rate capability for lithium-ion batteries. Carbon 148:518–524. https://doi.org/10.1016/j.carbon.2019.03.053

4. Larcher D, Tarascon JM (2015) Towards greener and more sustainable batteries for electrical energy storage. Nat Chem 7:19–29. https://doi.org/10.1038/nchem.2085

5. Lu Y, Yu L, Lou XW (2018) Nanostructured conversion-type anode materials for advanced lithium-ion batteries. Chem 4:972–996. https://doi.org/10.1016/j.chempr.2018.01.003

6. Tarascon JM, Armand M (2001) Issues and challenges facing rechargeable lithium batteries. Nature 414:359–367. https://doi.org/10.1038/35104644

7. Zhou Y, Tian J, Xu H, Yang J, Qian Y (2017) VS4 nanoparticles rooted by a-C coated MWCNTs as an advanced anode material in lithium ion batteries. Energy Storage Materials 6:149–156. https://doi.org/10.1016/j.ensm.2016.10.010

8. Yin L, Chai S, Ma J, Huang J, Kong X, Bai P, Liu Y (2017) Effects of binders on electrochemical properties of the SnS2 nanostructured anode of the lithium-ion batteries. J Alloy Compd 698:828–834. https://doi.org/10.1016/j.jallcom.2016.12.215

9. Bhandavat R, David L, Singh G (2012) Synthesis of surface-functionalized WS2 nanosheets and performance as li-ion battery anodes. J Phys Chem Lett 3:1523–1530. https://doi.org/10.1021/jz300480w

10. Youn DH, Jo C, Kim JY, Lee J, Lee JS (2015) Ultrafast synthesis of MoS2 or WS2-reduced graphene oxide composites via hybrid microwave annealing for anode materials of lithium ion batteries. J Power Sources 295:228–234. https://doi.org/10.1016/j.jpowsour.2015.07.013

11. Wang D, Liu Y, Meng X, Wei Y, Zhao Y, Pang Q, Chen G (2017) Two-dimensional VS2 monolayers as potential anode materials for lithium-ion batteries and beyond: first-principles calculations. J Materials Chem A 5:21370–21377. https://doi.org/10.1039/C7TA06944H

12. Seo J-w, Jang J-t, Park S-w, Kim C, Park B, Cheon J (2008) Two-dimensional SnS2 nanoplates with extraordinary high discharge capacity for lithium ion batteries. Adv Mater 20:4269–4273. https://doi.org/10.1002/adma.200703122

13. Momma T, Shiraishi N, Yoshizawa A, Osaka T, Gedanken A, Zhu J, Sominski L (2001) SnS2 anode for rechargeable lithium battery. J Power Sources 97–98:198–200. https://doi.org/10.1016/S0378-7753(01)00723-6

14. Zhong H, Yang G, Song H, Liao Q, Cui H, Shen P, Wang C-X (2012) Vertically aligned graphene-like SnS2 ultrathin nanosheet arrays: excellent energy storage, catalysis, photoconduction, and field-emitting performances. The J Physical Chem C 116:9319–9326. https://doi.org/10.1021/jp301024d

15. Liu Y, Yu X-Y, Fang Y, Zhu X, Bao J, Zhou X, Lou XW (2018) Confining SnS2 ultrathin nanosheets in hollow carbon nanostructures for efficient capacitive sodium storage. Joule 2:725–735. https://doi.org/10.1016/j.joule.2018.01.004

16. Jiang Y, Feng Y, Xi B, Kai S, Mi K, Feng J, Zhang J, Xiong S (2016) Ultrasmall SnS2 nanoparticles anchored on well-distributed nitrogen-doped graphene sheets for Li-ion and Na-ion batteries. J Materials Chem A 4:10719–10726. https://doi.org/10.1039/C6TA03580A

17. Du N, Wu X, Zhai C, Zhang H, Yang D (2013) Large-scale synthesis and application of SnS2–graphene nanocomposites as anode materials for lithium-ion batteries with enhanced cyclic performance and reversible capacity. J Alloy Compd 580:457–464. https://doi.org/10.1016/j.jallcom.2013.06.079

18. Zhang L, Huang Y, Zhang Y, Fan W, Liu T (2015) Three-dimensional nanoporous graphene-carbon nanotube hybrid frameworks for confinement of SnS2 nanosheets: flexible and binder-free papers with highly reversible lithium storage. ACS Appl Mater Interfaces 7:27823–27830. https://doi.org/10.1021/acsami.5b09115

19. Wang J, Luo C, Mao J, Zhu Y, Fan X, Gao T, Mignerey AC, Wang C (2015) Solid-state fabrication of SnS2/C nanospheres for high-performance sodium ion battery anode. ACS Appl Mater Interfaces 7:11476–11481. https://doi.org/10.1021/acsami.5b02413

20. Zhou Y, Wang Q, Zhu X, Jiang F (2018) Three-dimensional SnS decorated carbon nano-networks as anode materials for lithium and sodium ion batteries. Nanomaterials 8:135. https://doi.org/10.3390/nano8030135

21. Zhou Y, Yan D, Xu H, Liu S, Yang J, Qian Y (2015) Multiwalled carbon nanotube@a-C@Co9S8 nanocomposites: a high-capacity and long-life anode material for advanced lithium ion batteries. Nanoscale 7:3520–3525. https://doi.org/10.1039/c4nr07143c

22. Youn DH, Stauffer SK, Xiao P, Park H, Nam Y, Dolocan A, Henkelman G, Heller A, Mullins CB (2016) Simple synthesis of nanocrystalline tin sulfide/N-doped reduced graphene oxide composites as lithium ion battery anodes. ACS Nano 10:10778–10788. https://doi.org/10.1021/acsnano.6b04214

23. Yin J, Cao H, Zhou Z, Zhang J, Qu M (2012) SnS2@reduced graphene oxide nanocomposites as anode materials with high capacity for rechargeable lithium ion batteries. J Mater Chem 22:23963–23970. https://doi.org/10.1039/C2JM35137D

24. Kim HS, Chung YH, Kang SH, Sung Y-E (2009) Electrochemical behavior of carbon-coated SnS2 for use as the anode in lithium-ion batteries. Electrochim Acta 54:3606–3610. https://doi.org/10.1016/j.electacta.2009.01.030

25. Kosynkin DV, Higginbotham AL, Sinitskii A, Lomeda JR, Dimiev A, Price BK, Tour JM (2009) Longitudinal unzipping of carbon nanotubes to form graphene nanoribbons. Nature 458:872–876. https://doi.org/10.1038/nature07872

26. Domnich V, Reynaud S, Haber RA, Chhowalla M (2011) Boron carbide: structure, properties, and stability under stress. J Am Ceram Soc 94:3605–3628. https://doi.org/10.1111/j.1551-2916.2011.04865.x

27. Song S, Xu W, Cao R, Luo L, Engelhard MH, Bowden ME, Liu B, Estevez L, Wang C-M, Zhang J-G (2017) B4C as a stable non-carbon-based oxygen electrode material for lithium-oxygen batteries. Nano Energy 33:195–204. https://doi.org/10.1016/j.nanoen.2017.01.042

28. Song N, Gao Z, Zhang Y, Li X (2019) B4C nanoskeleton enabled, flexible lithium-sulfur batteries. Nano Energy 58:30–39. https://doi.org/10.1016/j.nanoen.2019.01.018

29. Wang C, Guo Z, Shen W, Xu Q, Liu H, Wang Y (2014) B-doped carbon coating improves the electrochemical performance of electrode materials for Li-ion batteries. Adv Func Mater 24:5511–5521. https://doi.org/10.1002/adfm.201401006

30. Chen X, Li X, Ding F, Xu W, Xiao J, Cao Y, Meduri P, Liu J, Graff GL, Zhang J-G (2012) Conductive rigid skeleton supported silicon as high-performance li-ion battery anodes. Nano Lett 12:4124–4130. https://doi.org/10.1021/nl301657y

31. Sun Y, Yang Y, Shi X-L, Suo G, Lu S, Chen Z-G (2021) Self-standing and high-performance B4C/Sn/acetylene black@reduced graphene oxide films as sodium-ion half/full battery anodes. Applied Materials Today 24:101137. https://doi.org/10.1016/j.apmt.2021.101137

32. Zhang E, Wang J, Wang B, Yu X, Yang H, Lu B (2019) Unzipped carbon nanotubes for aluminum battery. Energy Storage Materials 23:72–78. https://doi.org/10.1016/j.ensm.2019.05.030

33. Dimiev AM, Khannanov A, Vakhitov I, Kiiamov A, Shukhina K, Tour JM (2018) Revisiting the mechanism of oxidative unzipping of multiwall carbon nanotubes to graphene nanoribbons. ACS Nano 12:3985–3993. https://doi.org/10.1021/acsnano.8b01617

34. Deng L, Zhu J, Chen X, Ding M, Liu H (2018) Three-dimensional elastic ultrathin reduced graphene oxide coating SnS2 hierarchical microsphere as lithium ion batteries anode materials. J Alloy Compd 739:1015–1024. https://doi.org/10.1016/j.jallcom.2017.12.210

35. Zhang Q, Li R, Zhang M, Zhang B, Gou X (2014) SnS2/reduced graphene oxide nanocomposites with superior lithium storage performance. Electrochim Acta 115:425–433. https://doi.org/10.1016/j.electacta.2013.10.193

36. Zhang Y, Zhu P, Huang L, Xie J, Zhang S, Cao G, Zhao X (2015) Few-layered SnS2 on few-layered reduced graphene oxide as na-ion battery anode with ultralong cycle life and superior rate capability. Adv Func Mater 25:481–489. https://doi.org/10.1002/adfm.201402833

37. Fan J-J, Fan Y-J, Wang R-X, Xiang S, Tang H-G, Sun S-G (2017) A novel strategy for the synthesis of sulfur-doped carbon nanotubes as a highly efficient Pt catalyst support toward the methanol oxidation reaction. J of Materials Chem A 5:19467–19475. https://doi.org/10.1039/C7TA05102F

38. Sun W, Rui X, Yang D, Sun Z, Li B, Zhang W, Zong Y, Madhavi S, Dou S, Yan Q (2015) Two-dimensional tin disulfide nanosheets for enhanced sodium storage. ACS Nano 9:11371–11381. https://doi.org/10.1021/acsnano.5b05229

39. Yu J, Xu CY, Ma FX, Hu SP, Zhang YW, Zhen L (2014) Monodisperse SnS(2) nanosheets for high-performance photocatalytic hydrogen generation. ACS Appl Mater Interfaces 6:22370–22377. https://doi.org/10.1021/am506396z

40. Zhai C, Du N, Zhang H, Yu J, Yang D (2011) Multiwalled carbon nanotubes anchored with SnS2 nanosheets as high-performance anode materials of lithium-ion batteries. ACS Appl Mater Interfaces 3:4067–4074. https://doi.org/10.1021/am200933m

41. Zhang R, Chi C, Wu M, Liu K, Zhao T (2020) A long-life Li–S battery enabled by a cathode made of well-distributed B4C nanoparticles decorated activated cotton fibers. J of Power Sources 451:227751. https://doi.org/10.1016/j.jpowsour.2020.227751

42. Zhang YC, Yao L, Zhang G, Dionysiou DD, Li J, Du X (2014) One-step hydrothermal synthesis of high-performance visible-light-driven SnS2/SnO2 nanoheterojunction photocatalyst for the reduction of aqueous Cr(VI). Appl Catal B 144:730–738. https://doi.org/10.1016/j.apcatb.2013.08.006

43. Zheng P, Dai Z, Zhang Y, Dinh KN, Zheng Y, Fan H, Yang J, Dangol R, Li B, Zong Y, Yan Q, Liu X (2017) Scalable synthesis of SnS2/S-doped graphene composites for superior Li/Na-ion batteries. Nanoscale 9:14820–14825. https://doi.org/10.1039/C7NR06044K

44. Liu H, Chen X, Deng L, Su X, Guo K, Zhu Z (2016) Preparation of ultrathin 2D MoS2/graphene heterostructure assembled foam-like structure with enhanced electrochemical performance for lithium-ion batteries. Electrochim Acta 206:184–191. https://doi.org/10.1016/j.electacta.2016.04.160

45. Wang J-G, Sun H, Liu H, Jin D, Zhou R, Wei B (2017) Edge-oriented SnS2 nanosheet arrays on carbon paper as advanced binder-free anodes for Li-ion and Na-ion batteries. J Materials Chem A 5:23115–23122. https://doi.org/10.1039/C7TA07553G

46. Yu Z, Li X, Yan B, Xiong D, Yang M, Li D (2017) Rational design of flower-like tin sulfide @ reduced graphene oxide for

high performance sodium ion batteries. Mater Res Bull 96:516–523. https://doi.org/10.1016/j.materresbull.2017.04.048

47. Qu B, Ma C, Ji G, Xu C, Xu J, Meng YS, Wang T, Lee JY (2014) Layered SnS2-Reduced graphene oxide composite – a high-capacity, high-rate, and long-cycle life sodium-ion battery anode material. Adv Mater 26:3854–3859. https://doi.org/10.1002/adma.201306314

48. Yusuf M, Khan MA, Abdullah EC, Elfghi M, Hosomi M, Terada A, Riya S, Ahmad A (2016) Dodecyl sulfate chain anchored mesoporous graphene: synthesis and application to sequester heavy metal ions from aqueous phase. Chem Eng J 304:431–439. https://doi.org/10.1016/j.cej.2016.06.109

49. Wang X, Zhang Y, Chen H, Sun G, Wang Z, Hou H, Hu Z, Gao Q, Zhang Q (2022) High-capacity and cycling-stable anode for sodium ion batteries constructed from SnS2/MWCNTs nanocomposites. J Alloys Compounds 897:163029. https://doi.org/10.1016/j.jallcom.2021.163029

50. Wang G, Peng J, Zhang L, Zhang J, Dai B, Zhu M, Xia L, Yu F (2015) Two-dimensional SnS2@PANI nanoplates with high capacity and excellent stability for lithium-ion batteries. J Materials Chem A 3:3659–3666. https://doi.org/10.1039/C4TA06384H

51. Jiang X, Yang X, Zhu Y, Shen J, Fan K, Li C (2013) In situ assembly of graphene sheets-supported SnS2 nanoplates into 3D macroporous aerogels for high-performance lithium ion batteries. J Power Sources 237:178–186. https://doi.org/10.1016/j.jpowsour.2013.03.048

52. Du Y, Yin Z, Rui X, Zeng Z, Wu X-J, Liu J, Zhu Y, Zhu J, Huang X, Yan Q, Zhang H (2013) A facile, relative green, and inexpensive synthetic approach toward large-scale production of SnS2 nanoplates for high-performance lithium-ion batteries. Nanoscale 5:1456–1459. https://doi.org/10.1039/C2NR33458E

53. Zhao Y, Li X, Yan B, Li D, Lawes S, Sun X (2015) Significant impact of 2D graphene nanosheets on large volume change tin-based anodes in lithium-ion batteries: a review. J Power Sources 274:869–884. https://doi.org/10.1016/j.jpowsour.2014.10.008

54. Jana MK, Rajendra HB, Bhattacharyya AJ, Biswas K (2014) Green ionothermal synthesis of hierarchical nanostructures of SnS2 and their Li-ion storage properties. CrystEngComm 16:3994–4000. https://doi.org/10.1039/C3CE42561D

55. Zhai C, Du N, Yang HZD (2011) Large-scale synthesis of ultrathin hexagonal tin disulfide nanosheets with highly reversible lithium storage. Chem Commun 47:1270–1272. https://doi.org/10.1039/C0CC03023F

56. Guo J, Li Y, Meng J, Pedersen K, Gurevich L, Stroe D-I (2022) Understanding the mechanism of capacity increase during early cycling of commercial NMC/graphite lithium-ion batteries. J Energy Chem 74:34–44. https://doi.org/10.1016/j.jechem.2022.07.005

57. He Y, Wang L, Dong C, Li C, Ding X, Qian Y, Xu L (2019) In-situ rooting ZnSe/N-doped hollow carbon architectures as high-rate and long-life anode materials for half/full sodium-ion and potassium-ion batteries. Energy Storage Materials 23:35–45. https://doi.org/10.1016/j.ensm.2019.05.039

58. Hu M, Jing H, Li T, Wang J, Yang H, Lv R, Chen D (2019) Composite K2Mo4O13/α-MoO3 nanorods: sonochemical preparation and applications for advanced Li+/Na+ pseudocapacitance. J Materials Chem A 7:10954–10961. https://doi.org/10.1039/C8TA11854J

59. Costentin C (2020) Electrochemical energy storage: questioning the popular v/v1/2 scan rate diagnosis in cyclic voltammetry. The J Physical Chem Lett 11:9846–9849. https://doi.org/10.1021/acs.jpclett.0c02667

60. Cheng Y, Huang J, Li J, Xu Z, Cao L, Ouyang H, Yan J, Qi H (2016) SnO2/super P nanocomposites as anode materials for Na-ion batteries with enhanced electrochemical performance. J Alloy Compd 658:234–240. https://doi.org/10.1016/j.jallcom.2015.10.212

61. Chen X, Huang Y, Zhang K, Feng X, Wang M (2017) Synthesis and high-performance of carbonaceous polypyrrole nanotubes coated with SnS2 nanosheets anode materials for lithium ion batteries. Chem Eng J 330:470–479. https://doi.org/10.1016/j.cej.2017.07.180

62. Xia J, Liu L, Xie J, Yan H, Yuan Y, Chen M, Huang C, Zhang Y, Nie S, Wang X (2018) Layer-by-layered SnS2/graphene hybrid nanosheets via ball-milling as promising anode materials for lithium ion batteries. Electrochim Acta 269:452–461. https://doi.org/10.1016/j.electacta.2018.03.022

63. Hassan FM, Hu Q, Fu J, Batmaz R, Li J, Yu A, Xiao X, Chen Z (2017) Hot-chemistry structural phase transformation in single-crystal chalcogenides for long-life lithium ion batteries. ACS Appl Mater Interfaces 9:20603–20612. https://doi.org/10.1021/acsami.7b04483

64. Hu Q, Wang B, Chang S, Yang C, Hu Y, Cao S, Lu J, Zhang L, Ye H (2021) Effects of annealing temperature on electrochemical performance of SnSx embedded in hierarchical porous carbon with N-carbon coating by in-situ structural phase transformation as anodes for lithium ion batteries. J Mater Sci Technol 84:191–199. https://doi.org/10.1016/j.jmst.2020.12.068